Modeling of InGaAsBi/InGaAs/InP Multi-Quantum Wells Short-Wave Infrared Detectors

Sfina N[*1,2], Ammar I[1], Brimi S[3,4] and Fnaiech M[1]

[1]Laboratoire de la Matière Condensée et des Nanosciences (LMCN), Département de Physique, Faculté des Sciences de Monastir, Université de Monastir, Avenue de l'Environnement, 5019 Monastir, Tunisia
[2]Faculty of Science and Art KKU Mahail Assir, King Khalid University, Saudi Arabia
[3]Department of Mathematics, College of Science, Imam Abdulrahman Bin Faisal University, Dammam, Saudi Arabia
[4]Basic and Applied Scientific Research Center, Imam Abdulrahman Bin Faisal University, Dammam, Saudi Arabia

[*]**Corresponding author:** Sfina N, Laboratoire de la Matière Condensée et des Nanosciences (LMCN), Département de Physique, Faculté des Sciences de Monastir, Université de Monastir, Avenue de l'Environnement, 5019 Monastir, Tunisia and Faculty of Science and Art KKU Mahail Assir, King Khalid University, Saudi Arabia, Tel: +21621325107, E-mail: sfina_fsm@yahoo.fr

Abstract

We report the theoretical investigation of type-I InGaAsBi/InGaAs superlattice short-wave infrared detector nearly lattice matched to InP substrate such as the quaternary InGaAsBi/InGaAs layer is the absorption region. The used bismuth composition is about 5.5%, the Bi incorporation induced a cut-off wavelength red-shift from 1.6 μm to 3μm at room temperature (RT), and showing a band gap reduction about 362meV. The electron transport in the $In_{0.53}Ga_{0.47}As_{0.945}5Bi_{0.055}/In_{0.53}Ga_{0.47}As/InP$ multi-quantum wells-based p–i–n structure was investigated and numerically simulated taking on consideration tunneling process and thermally activated transfer through the barriers mostly. The temperature dependence of dark current density and zero-bias resistance area product (R_0A) has been examined. Take out from current–voltage characteristics, R_0A products exceeding to $1.62 \times 10^7 \Omega$ cm^2 and quantum efficiency (QE) of 33.35% at 77 K, achieving with an explicit detectivity around 2.24×10^{11} cmHz$^{1/2}$W^{-1}. The detector indicates a reassuring dark current density of 5.38×10^{-5}A/cm^2 at reverse bias voltage of 10mV at 300 K. These results approved the encouraging potential of InGaAsBi/InGaAs detectors nearly lattice matched to InP substrate for shortwave infrared detection.

Keywords: Dilute-Bismide Band Structure Engineering; Multi-Quantum wells p-i-n Structure; Short-wave Infrared Detection; Dark Current; Quantum Efficiency; Detectivity

Introduction

The incorporation of bismuth into III-V semiconductors materials, have attracted match interest due to their interesting properties of band gap reduction and the increasing of spin-orbit splitting energy [1-5]. The Addition of small fraction of bismuth in III-V semiconductors layer generates an energy state localized in the valence band as a perturbation, the interaction of the localized Bi level and the extended valence band states indications to an anti-crossing (VBAC) of these two states [6]. This powerfully decreases Bi atoms and increasing the up shift of the maximum in valence band. Firstly the important reduction of the band gap is of the order of ~56 meV/Bi% in InGaAsBi, [7] and opens the way to extend the spectral range of optoelectronics emission and detection devices based on GaAs and InP in the mid-infrared range. On the other hand, adding bismuth substantially increases the spin–orbit splitting energy segregation, Δ_{SO} [8]. This is by dint of both the properties of an enhanced electron spin–orbital (SO) angular momentum exchange within the heavy bismuth atoms and the skyward shift of the valence band maximum. These procedures makes bismide alloys promising for long wavelength cover a spectral range from the near- and mid-infrared photonic devices. The integration of bismuth propositions the potential for narrow band gap materials through a large spin-orbit splitting. In recent years, many researchers have reported the growth and characterization of some III-V-Bi combinations, by the incorporation of arsenides and antimonides on GaAsBi material [9,10]. Nevertheless, so as to achievement the advantageous proprieties of the dilute bismide material system, confirmation of great performance optoelectronic devices is essential. In the field of detection devices, same recent works they showed the performance of the incorporation of dilute bismide on In(As)SbBi/InSb for far infrared application [11]. In addition, there are new designed detectors have been realized using, GaAsBi/GaAs and InAsBi/InAs who's the cut-off wavelengths are 1.03 μm and 3.95 μm, respectively [12,13]. In order to improve the device performance all these detectors are designed with active materials lattice mismatched to their respective substrates. The research and development of InGaAs technology shows that the InGaAs allows us to create products that see infrared waves, in particular short-wave infrared (SWIR, 1-3 μm) devices. These detectors have many military and civilian application, such as night vision [14] and earth resource observation. In these devices, an InGaAs ($In_{0.53}Ga_{0.47}As$) layer with a band gap Eg of 0.75 eV at RT and a cutoff wavelength of around 1.67 μm is used as the absorption material, while lattice-matched to InP substrate, but the disadvantage of this material system still remains the large lattice mismatch and great threading dislocation density [15,16]. In order to overcome the suffering of this materials system and increases the cutoff wavelength, Petropoulos et al [17] shown that the bandgap of the quaternary alloy InGaAsBi is reduced by the integration of Bi by about -50 meV/% Bi. Moreover, $In_{0.53}Ga_{0.47}As_{1-x}Bi_{x}$ layer can be grown nearly lattice matched to InP substrate, who proves a significant advantage for detectors devices [18]. The high-quality of the growth parameters of the quaternary InGaAsBi materials nearly lattice matched to InP have been carried out for a Bi concentration up to 6.75 % [19, 20]. Due to both the improvement of device performance and the high–quality of materials growth InGaAsBi is a promising material for SWIR applications. Consequently, it is possible to realize practically the device in which the absorption layer is made with MQWs InGaAsBi/InGaAs/InP.

Furthermore, two years ago, an infrared InGaAsBi detector grown on InP substrate was studied by Gu *et al* [21]. The former structure was provided with the quaternary InGaAsBi absorption layer leading to a 50% cut-off wavelength and to a bandgap reduction of about 180 meV at room temperature. In addition, Gu *et al* measured a dark current density of 2.4×10^{-4} A/cm^2 at a bias voltage of -10 mV which is lower than what found in previous works giving perspectives for further better wavelength cut-off. Hence, it was demonstrated by Gu *et al* that the resistance area product R_0A of the detector increases as the temperature decreases. All these previous results make encouraging pushing forward research for better photodetector performance. These detectors have large applications fields within remote sensing, environmental monitoring, and night vision [22-26].

In this work, we report the optimization and, the theoretical investigation of a MQWs InGaAsBi/InGaAs/InP p-i-n detector which is nearly lattice matched to an InP substrate operating at RT around 2.6μm. So as to design such device, it is very significant to known the optoelectronic characteristics of strained InGaAsBi, such as band gap energy and bands offsets versus of Bi fraction as well as the large modification of the spin-orbit splitting energy. The active absorption layer of the detector under investigated consists of ten InGaAsBi/InGaAs separated by 10-nm-thick InP spacers. We analyzed dark current participating mechanisms over

the temperature dependence of zero-bias resistance area product (R_0A) and the temperature dependence performance is finally introduced and discussed in terms of quantum efficiency, detectivity and responsivity.

Modeling parameters

The Knowledge of strained band gaps and band discontinuities are among the main parameters for the design of optoelectronics devises. In addition, the energy of the band gaps allows us to determine the operating wavelength, although the band offsets control the carrier transport and the performance of designed devices. In this way, we have calculated these parameters for $In_yGa_{1-y}As_xBi_{1-x}$ as a function of correlated compositions. Energy-band structure calculation, Photo-reflectance (PR) photoluminescence (PL), experiments and absorption at (RT) [7], have chosen that the band gap of $In_yGa_{1-y}As_xBi_{1-x}$ alloys illustrate that the integration of bismuth atoms into InGaAs host affects both the valence and conduction bands. The experimental results given by Petropoulos et al prove that the band gap of InGaAsBi is reduced by the integration of Bi by about -50 meV/% Bi, which is considerably larger than about -10meV/% In for InGaAs material [27]. The bandgap and spin-orbit splitting energy versus Bi fraction and temperature have been studied by Spectro-Photometry (SP), (PL), (PR), and contactless Electrore Flectance (EF) [28-30]. The thermoelectric applications of InGaAsBi and the InGaAsBi quantum wells have also been investigated [31,32]. The relaxed band gap energy of the quadratic quaternary alloy $In_yGa_{1-y}As_xBi_{1-x}$ can be calculated from the following equation [33].

$$E_g^{In_yGa_{1-y}As_xBi_{1-x}}(x,y) = \frac{E_{g1}(x,y)+E_{g2}(x,y)}{x(1-x)+y(1-y)} \tag{1}$$

$$E_{g1}(x,y) = x(1-x)\left[y\, E_g^{InAs_{1-x}Bi_x} + (1-y)\, E_g^{GaAs_{1-x}Bi_x}\right] \tag{2}$$

$$E_{g2}(x,y) = y(1-y)\left[x\, E_g^{In_yGa_{1-y}Bi} + (1-x)E_g^{In_yGa_{1-y}As}\right] \tag{3}$$

$$E_g^{InAs_{1-x}Bi_x} = x\, E_g^{InBi} + (1-x)E_g^{InAs} - b_0 x(1-x) \tag{4}$$

$$E_g^{GaAs_{1-x}Bi_x} = x\, E_g^{GaBi} + (1-x)E_g^{GaAs} - b_1 x(1-x) \tag{5}$$

$$E_g^{In_yGa_{1-y}Bi} = y\, E_g^{InBi} + (1-y)E_g^{GaBi} - b_2 y(1-y) \tag{6}$$

$$E_g^{In_yGa_{1-y}As} = y\, E_g^{InAs} + (1-y)E_g^{GaAs} - b_3 y(1-y) \tag{7}$$

$$E_{g1}(x,y) = x(1-x)\left[y\left[x\, E_g^{InBi} + (1-x)E_g^{InAs} - b_0 x(1-x)\right] + (1-y)\left[x\, E_g^{GaBi} + (1-x)E_g^{GaAs} - b_1 x(1-x)\right]\right] \tag{8}$$

$$E_{g2}(x,y) = y(1-y)\left[x\left[y\, E_g^{InBi} + (1-y)E_g^{GaBi} - b_2 y(1-y)\right] + (1-x)\left[y\, E_g^{InAs} + (1-y)E_g^{GaAs} - b_3 y(1-y)\right]\right] \tag{9}$$

where b_i $(i = 0,1,2,3)$ and E_g^j $(j = InBi, InAs, GaBi, GaAs)$ are the bowing parameters and the band gaps of used materials respectively.

Material	$b_0 = b_{inBi-InAs}$	$b_1 = b_{GaBi-GaAs}$	$b_2 = b_{InBi-GaBi}$	$b_3 = b_{INAs-GaAs}$
Bowing parameters(eV)	0.583 [34]	1.74 [35]	0.45 [36]	0.45 [36]

Table 1: Bowing parameters of the used materials [34-36]

Parameters	GaAs	GaBi	InAs	InBi
a (Å)	5.6532	6.3280	6.0584	6.6860
$E_g^{\Gamma}(eV)$	1.42	-1.45	0.35	-1.63
$E_g^{X}(eV)$	1.98	-	1.43	-
$E (eV)$	1.72	-	1.13	-
$\Delta_0(eV)$	0.34	2.2	0.38	2.24/2.15
$C_{11}(GPa)$	1.18	81.6	0.83	58.5
$C_{12}(GPa)$	0.54	28.1	0.45	30.4
$a_V(eV)$	1.16	1.16	1.00	1.00
$a_c(eV)$	-7.17	−8.06	-5.08	−5.88
$b(eV)$	-1.7	−1.70	-1.80	−1.80
γ_1	6.85	-	20.40	-
γ_2	2.1	-	20.4	-
m_e^*/m_0	0.0630	0.0655	0.0230	0.026
$a_{v,av}(eV)$	-6.92	-6.28	-6.67	-6.15

Table 2: Material parameters used in the calculations

at 300 K. They are taken from References [1-16]

Using the parameters listed in Tables 1 and 2 we have calculated the relaxed band gap expressions as the function of x and y compositions

$$E_{g1}(x,y) \approx x(1-x)\left[y[0.356 - 2.569x + 0.583x^2] + (1-y)[1.519 - 4.709x + 0.583x^2]\right]$$ (10)

$$E_{g2}(x,y) \approx y(1-y)\left[x[-1.45 - 0.63y + 0.45y^2] + (1-x)[1.519 - 1.689y + 0.45y^2]\right]$$ (11)

Using Vegard's law and the linear interpolation of the lattice constant of the four point binaries, the lattice constant of the $In_yGa_{1-y}As_xBi_{1-x}$ is obtained with the formula

$$a_{In_yGa_{1-y}As_xBi_{1-x}} = a_{GaAs}(1-y)(1-x) + a_{InAs}y(1-x) + a_{GaBi}x(1-y) + a_{InBi}xy$$ (12)

From the band gap and the lattice constant expressions as can be seen that, $In_yGa_{1-y}As_xBi_{1-x}$ can be grown lattice matched to InP for $y = 0.53 - 1.5601x$, which is an significant benefit for optoelectronics devices.

In order to study the band alignment through (001)–oriented $In_yGa_{1-y}As_xBi_{1-x}$/InP strained interfaces, we have calculated the relative alignment of the band profiles between the $In_yGa_{1-y}As_xBi_{1-x}$ and the InP layers using the model-solid theory given by Van de Walle et al [37, 38]. This model is applied and can be used for lattice-matched and lattice-mismatched interfaces. To calculate the band offset we considerate the $E_{V,av}$ which represents the energy location level for valence band defined as the average over the highest valence band at the Γ-point of the Brillouin zone. which the valence band edge is given by equation (12) for heavy holes

$$E_V = \begin{cases} E_{V,av} + \frac{\Delta_0}{3} + \delta E_{V,hh} \\ E_{V,av} + \frac{\Delta_0}{3} + \delta E_{V,lh} \end{cases}$$ (13)

where Δ_{SO} is the spin-orbit splitting energy, $E_{V,av}$ is the energy reference level in valence band-edge and $\delta E_{V,hh}$ and $\delta E_{V,lh}$ are the shift of the strained bulk valence band edge corresponding to the unstrained one, that shows to the splitting of the valence band into heavy-hole and light-hole subbands respectively. In our calculations we have taken into account the shifts caused by induced strain at levels of the conduction band, valence band minimum and maximum respectively . The energy displacements of the band are related to the deformations by using the deformation potentials. The band discontinuities are presented for unstrained materials as depicted in Figure 1. The band offset shift is due the lattice-mismatched interfaces and it is further global approach than a definition of band discontinuities for strained materials to designate the obtained band structure of semiconductor materials. The strain effect improves the quantum confinement for electrons and holes, this modification as presented schematically in Figure 1. For strain along the [001] direction of the $In_yGa_{1-y}As_xBi_{1-x}$/InP heterostructure, the shifts of the conduction and valence bands are assumed by the following expressions outlines in reference [39].
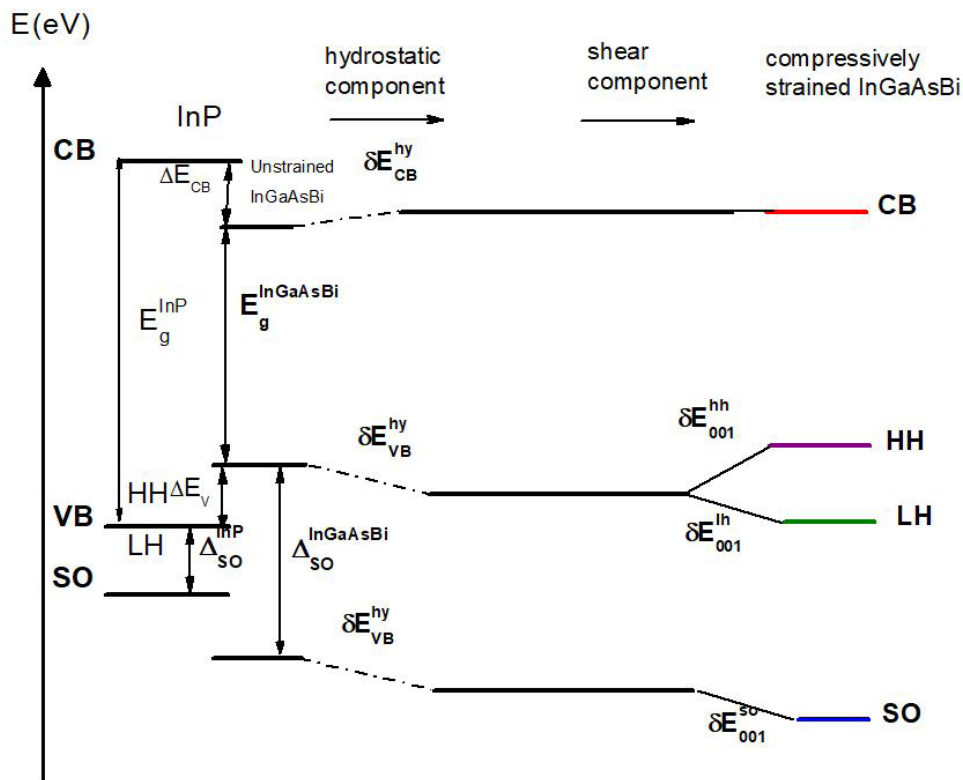

Figure 1: Bandgap alignment at the $In_yGa_{1-y}As_xBi_{1-x}$/InP interface: definition of the VBO at the unstrained $In_yGa_{1-y}As_xBi_{1-x}$/InP interface and band offsets in the conduction and valence band in compressively strained $In_yGa_{1-y}As_xBi_{1-x}$/InP QWs

$$\delta E_C = 2a_C \varepsilon_{//}\left(1 - \frac{c_{12}}{c_{11}}\right) \tag{14}$$

$$\delta E_{V,hh} = 2a_V \varepsilon_{//}\left(1 - \frac{c_{12}}{c_{11}}\right) - \frac{1}{2}\delta E_{001} \tag{15}$$

$$\delta E_{V,lh} = 2a_V \varepsilon_{//}\left(1 - \frac{c_{12}}{c_{11}}\right) - \frac{\Delta_0}{2} + \frac{1}{4}\delta E_{001} + \frac{1}{2}\left[\Delta_0^2 + \Delta_0 \delta E_{001} + \frac{9}{4}(\delta E_{001})^2\right]^{1/2} \tag{16}$$

$$\delta E_{V,SO} = 2a_V \varepsilon_{//}\left(1 - \frac{c_{12}}{c_{11}}\right) + \frac{\Delta_0}{2} + \frac{1}{4}\delta E_{001} - \frac{1}{2}\left[\Delta_0^2 + \Delta_0 \delta E_{001} + \frac{9}{4}(\delta E_{001})^2\right]^{1/2} \tag{17}$$

$$\delta E_{001} = -2b\varepsilon_{//}\left(2\frac{c_{12}}{c_{11}} + 1\right) \tag{18}$$

$$\varepsilon_{//} = \frac{a_{//}}{a} - 1 \tag{19}$$

$$\varepsilon_{\perp} = -2\frac{C_{12}}{C_{11}}\varepsilon_{//} \tag{20}$$

$a_{//}$ and a are the substrate and the unstrained over-layer lattice constants while $a_\perp$ is the perpendicular over-layer lattice constant given, in the [001] direction, by

$$a_\perp = a\left\{1 - 2\frac{C_{12}}{C_{11}}\left(\frac{a_{//}}{a} - 1\right)\right\} \tag{21}$$

Where a_c and a_v are the hydrostatic deformation potential for the valence and conduction band respectively, Δ_0 is the spin–orbit splitting, b is the shear deformation potential for the valence band and C_{ij} specify the bulk elastic coefficients for the material below consideration. The values for a, a_c, C_{11} and C_{12} for $In_yGa_{1-y}As_{1-x}Bi_x$ are obtained by linear interpolation between those of the four end-point binary combinations GaAs, InAs, GaBi and InBi, as shown in Table 2, which is predictable to be a noble approximation for the dilute Bi structures below examination. The first and the second terms of the valence band offsets are the hydrostatic and the shear corrections respectively. Seeing that the hydrostatic component of the strain is the same for hh, lh and so. Equations (19) to (21) indicate that heavy holes keep uncoupled from light holes, though light holes and split bands are coupled by deformation and spin-orbit splitting. Accordingly, the conduction and valence band offset counting strain effects for the $In_yGa_{1-y}As_xBi_{1-x}$ /InP interfaces are

$$\Delta E_C = \Delta E_V^{uns} + \Delta E_g^{uns} + \delta E_C \tag{22}$$

$$\Delta E_V = \left[E_V^{uns}\left(In_yGa_{1-y}As_xBi_{1-x}\right) + \delta E_V^{hyd} + \delta E_V^{sh}\right] - E_V^{uns}(InP) \tag{23}$$

$$\Delta E_{V,hh,lh,so} = \Delta E_V^{uns} + \delta E_V^{hyd} + \delta E_V^{sh} \tag{24}$$

where ΔE_g^{uns} is the band gap of unstrained bulk materials given by the equation (1). The δE_V^{hyd} and δE_V^{sh} represents the hydrostatic and the shear components of the strain respectively. Using the above equations, we have revealed the band discontinuities for strained $In_yGa_{1-y}As_xBi_{1-x}$/InP for the range $0 \le x \le 0. 1$. All used parameters in the simulation are listed in Table 2. Figure 2a shows the predicted strained band gap of InGaAsBi on InP versus of bismuth fraction at various indium compositions of up to 60% at 300 K. The experimental results of $In_{0.53}Ga_{0.47}As_{1-x}Bi_x$ on InP measured at 300k by diverse techniques, such as photoluminescence (PL), photo-reflectance (PR) and absorption [7]. Figure 2b shown a recapitulation of the compositional dependence experimental data of Δ_{SO} and Eg in InGaAsBi with a fixed, indium concentration of 53% versus the Bi composition, these results are in good agreement with our theoretical calculation [7,8]. Based on these results, it is clear that the crossover energy between Δ_{SO} and Eg is obtained at Bi composition about (3–4) % in the InGaAsBi alloy system on InP. InGaAsBi/InP is appropriate for the near- and mid-IR, wave length principally, still upholding bearable, strain levels on InP substrate. Furthermore, for 3.2% bismuth integration to realized detector device, the cutoff wavelength is around 2.1 µm at RT [18]. While a small composition of Bi is needed to attain the favored band structure over indium as well as InGaAsBi/InP structures can exploit the well-established conventional InP telecom processing, and the fact that InP substrates are very much cheaper and more thermally conductive than GaSb as conservatively used for interband mid infrared devices. These results display the promising potential of the InGaAsBi/InP devices for mid-IR applications. Using the set of equations mentioned above, we have calculated $\Delta E_{V,hh}$, $\Delta E_{V,lh}$ and ΔE_C for $In_yGa_{1-y}As_xBi_{1-x}$/InP heterointerface versus x and y compositions of bismuth and indium respectively. Figure 3 illustrated the calculated band discontinuities, of the conduction (ΔE_C) and valence band for heavy-hole ($\Delta E_{V,hh}$) and light-hole ($\Delta E_{V,lh}$) of $In_yGa_{1-y}As_xBi_{1-x}$/InP versus Bi fraction with In compositions of 40%–60% at 300 K. The inset displays the band discontinuities of the lattice-matched $In_{0.53}Ga_{0.47}AsBi$ on InP. From the above results it can be seen that the incorporation of the bismuth fraction has a minor effect on(ΔE_C). Nevertheless the valence band discontinuities ($\Delta E_{V,hh}$ and$\Delta E_{V,lh}$) increase swiftly through the increasing of bismuth concentrations. This effect is due to the robust ascending move of the top of the valence band following the Bi incorporation.
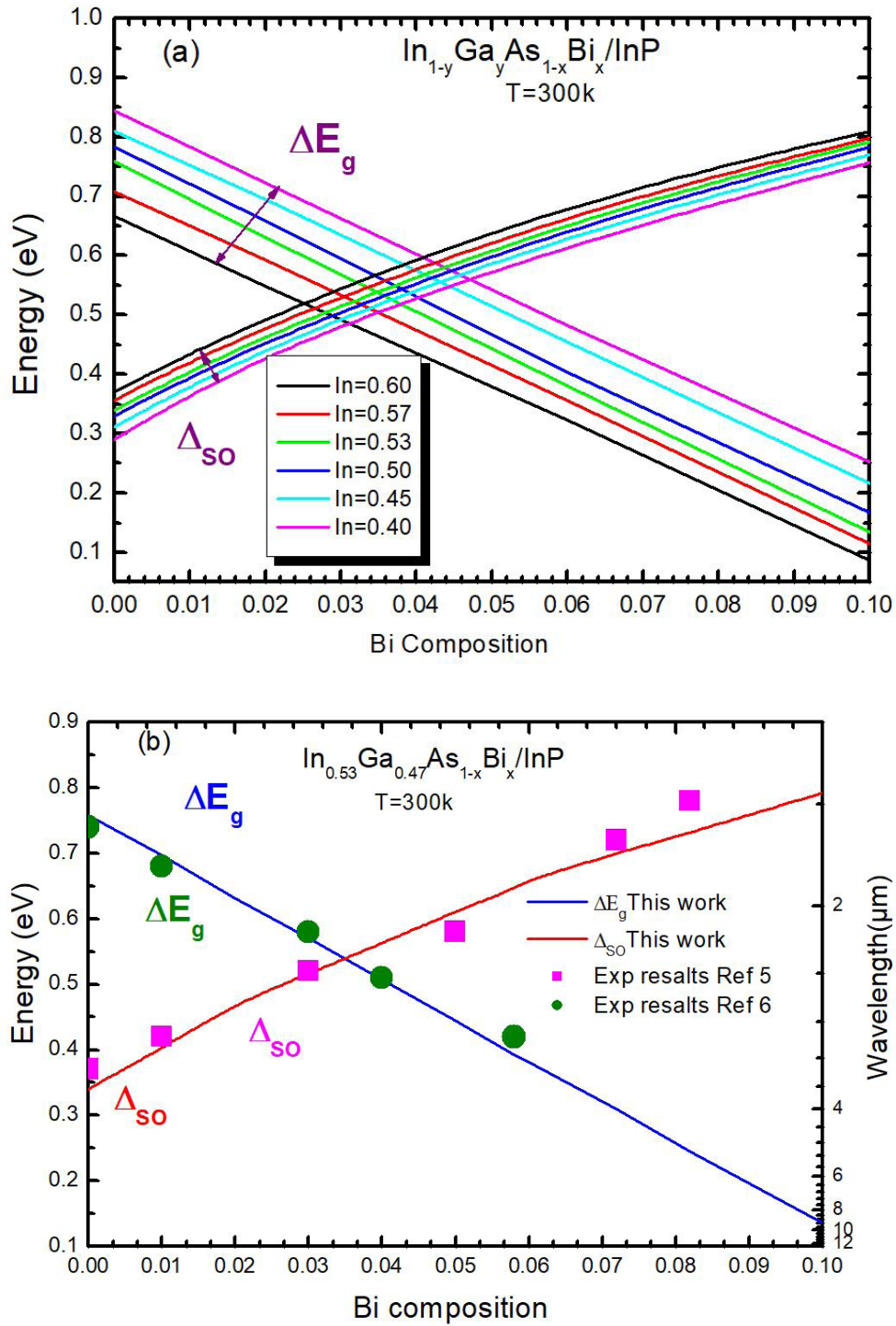
Figure 2: (a) Estimated band gap of InGaAsBi on InP at 300 K versus Bi concentration for same In compositions. The modification of spin-orbit splitting energy of InGaAsBi alloys is similarly represented; (b) The expected band gap and spin-orbit splitting energy of $In_{0.53}Ga_{0.47}As1_{-x}Bi_x$ on InP at 300k versus bismuth composition. The data points show the experimental results taken from ref [7] and [8]
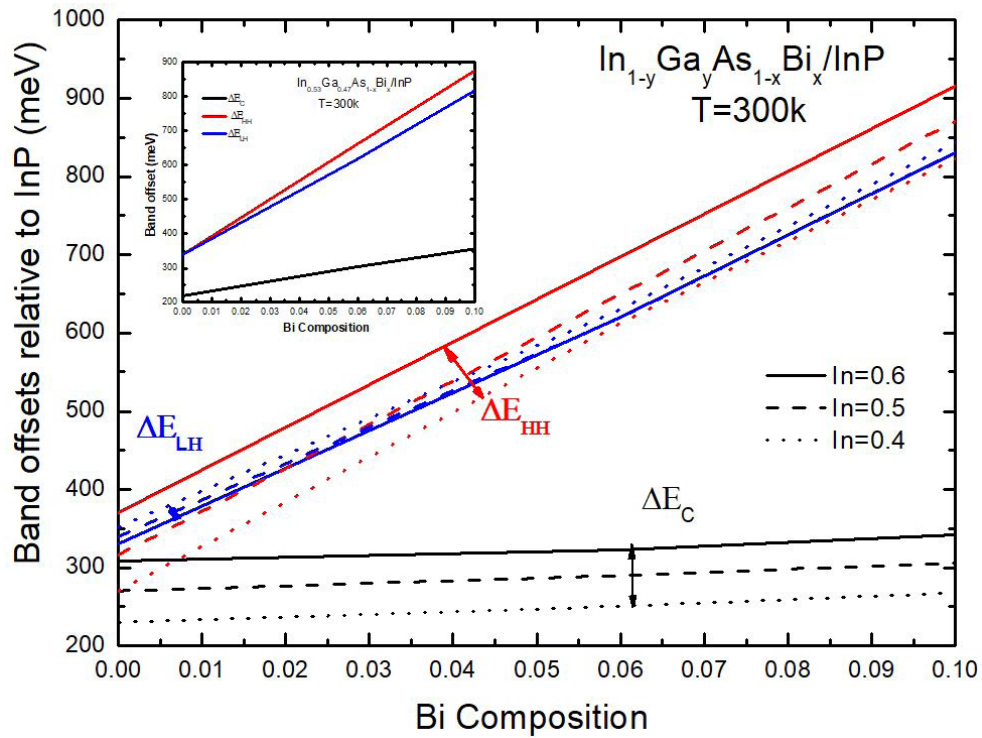
Figure 3: The estimated band discontinuities of InGaAsBi conduction band, heavy-hole and light-hole bands comparative to InP substrate versus bismuth composition at In fraction of 40%, 50%, and 60% at RT K. The inset displays the band discontinuities of the nearly lattice-matched $In_{0.53}Ga_{0.47}AsBi$ on InP at 300k

Same Theoretical and experimental results confirm that in GaAsBi system when the bismuth composition increase there is a short descending shift of the conduction band-profile [40]. The larger Bismuth atoms in GaAs leading to compressive strain, leading to an skyward displacement of the conduction band profile and consequently a reduction in ΔE_C. The addition of In atoms results in a larger conduction band shift. In the case of $In_yGa_{1-y}As_xBi_{1-x}$/InP ΔE_C is reduced that both $\Delta E_{V,hh}$ and $\Delta E_{V,lh}$. It is clearly visible that the increase in ΔE_C is mainly due to the increase in the indium fraction. In order to find an important a higher conduction band discontinuity in $In_yGa_{1-y}As_xBi_{1-x}$/InP, a greater In concentrations are required. Analyzing these results we can confirm good agreement between our calculation and the PR experiment results. For a strained $In_{0.53}Ga_{0.47}As_xBi_{1-x}$ on relaxed InP hetero-interface, the following approached analytical laws of the valence and conduction band discontinuities are mentioned as follows:

$$\Delta E_C^{\Gamma}(x) = 0.22 + 1.40343x - 0.33491x^2 \tag{25}$$

$$\Delta E_V^{hh}(x) = 0.34 + 5.3243x + 0.15052x^2 \tag{26}$$

$$\Delta E_V^{lh}(x) = 0.34 + 4.41974x + 3.55987x^2 \tag{27}$$

In this case energies are given in eV. The $In_{0.53}Ga_{0.47}As_xBi_{1-x}$/InP interfaces have type I alignments at Γ-Γ critical point, which indicates that electrons, heavy and light holes are confined into $In_{0.53}Ga_{0.47}As_xBi_{1-x}$ alloys. Figure 4 indicated the electronic band structure of $In_{0.53}Ga_{0.47}As_xBi_{1-x}$ with Bi composition about 5.5 % and the relative total and partial DOS of $In_{0.53}Ga_{0.47}As_{0.945}Bi_{0.055}$. The dark curve shows the total DOS and the contribution from each state is shown by (Color online) curves. These results are obtained from DFT calculations. The supercell with atom distribution found rendering to SQS and corresponding to composition examined in Figure 4 are presented in Figure 5. For a solid preliminary point of this study, the band structure of $In_{0.53}Ga_{0.47}As_{0.945}Bi_{0.055}$ is calculated and represented in Figure 4. The values of the gap and spin-orbit splitting energy of $In_{0.53}Ga_{0.47}As_{0.945}Bi_{0.055}$ is 0.413 eV and 0.634 eV respectively. These values are in perfect arrangement with experimental results [35]. From the representation of the band structure, can be seen that the conduction and valence band conserve the Bloch nature no changes to occur in this alloy. In bulk $In_{0.53}Ga_{0.47}As_{0.945}Bi_{0.055}$, the band structure is not undergone a significant change by the addition of a small fraction of Bi atoms
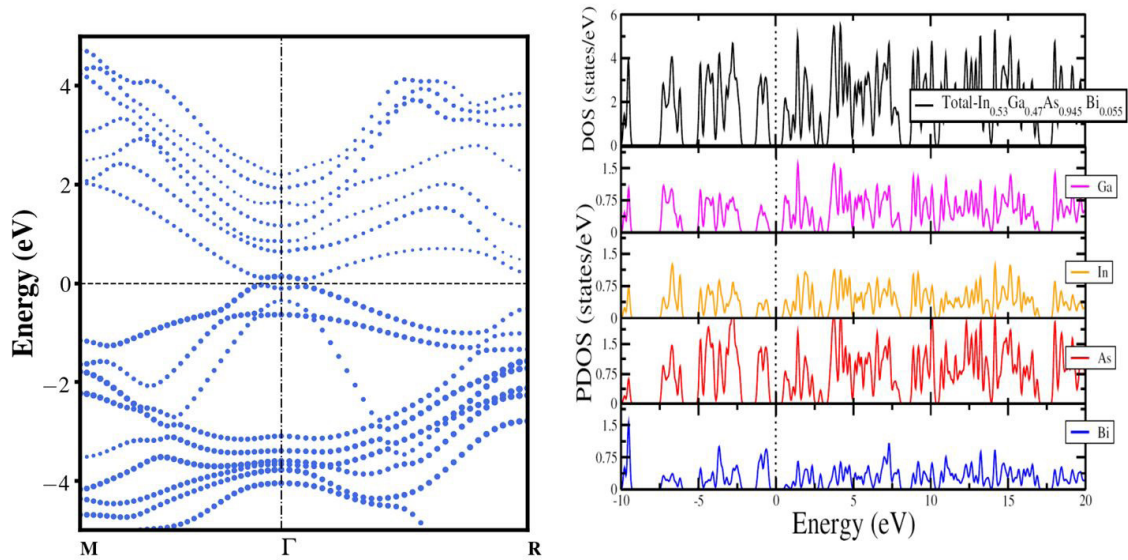
Figure 4: Electronic band structure of $In_{0.53}Ga_{0.47}As_xBi_{1-x}$ with Bi concentration about 5.5 % obtained by ab-initio calculation

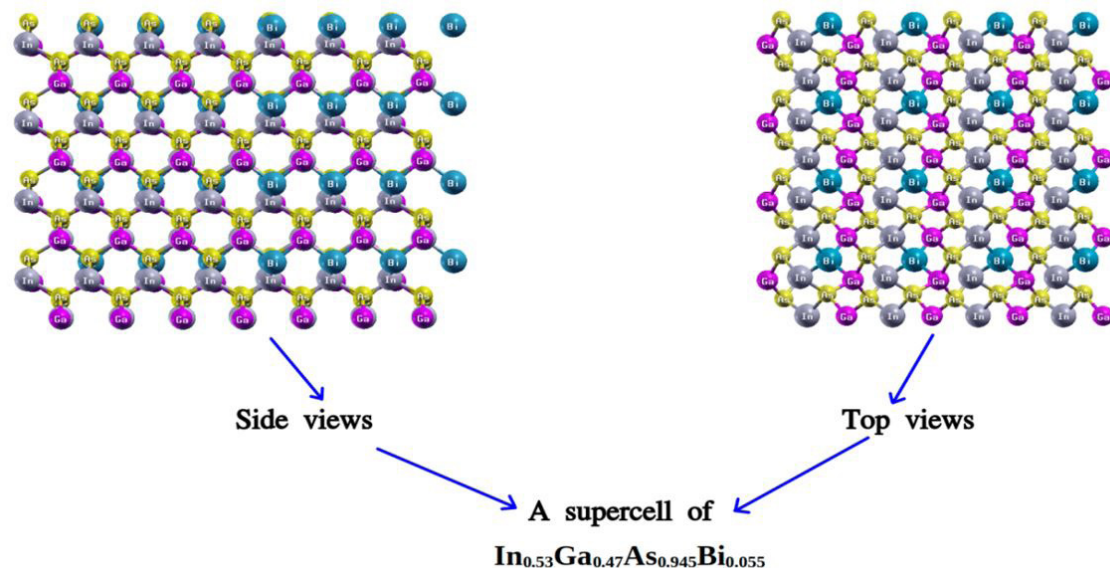**Figure 5:** A super cells of $In_{0.53}Ga_{0.47}As_{0.945}Bi_{0.055}$ with atom distribution according to side views and top views positions

Structure and design

The modulated and deigned detector heterostructure under investigation is made of ten periods of intrinsic $In_{0.53}Ga_{0.47}As_{0.945}Bi_{0.055}$ /$In_{0.53}Ga_{0.47}$ quantum wells both compressively strained $In_{0.53}Ga_{0.47}As_{0.945}Bi_{0.055}$ and $In_{0.53}Ga_{0.47}$ barriers are 26.5 nm thick. The active zone was inserted between tow 50 nm-thick InP layers. Be and Si were used as p- and n-type dopants, respectively. Using effective mass approximation, we have determined the quantum levels, the wave functions and the associated parameters. We have solved the one-dimensional Schrödinger equation according to the growth direction z supposing a steadily varying effective mass a Ben–Daniel– Duke Hamiltonian is applied [42]. The modeling parameters such as the effective masses in addition to the offsets in valence and conduction bands used in the simulation are outlined in section 2 and Tabe 2. From Figure 6 you can see that, the detection energy decreases when the $In_{0.53}Ga_{0.47}As_{0.945}Bi_{0.055}$ layer thickness decrease due to the increasing of electrons and heavy holes energy levels. In the inset is shown the Band edges, subband energies and the correspinding wave function components for one period of the $In_{0.53}Ga_{0.47}As_{0.945}Bi_{0.055}$/InP structure designed for 2.6μm wave length detection.
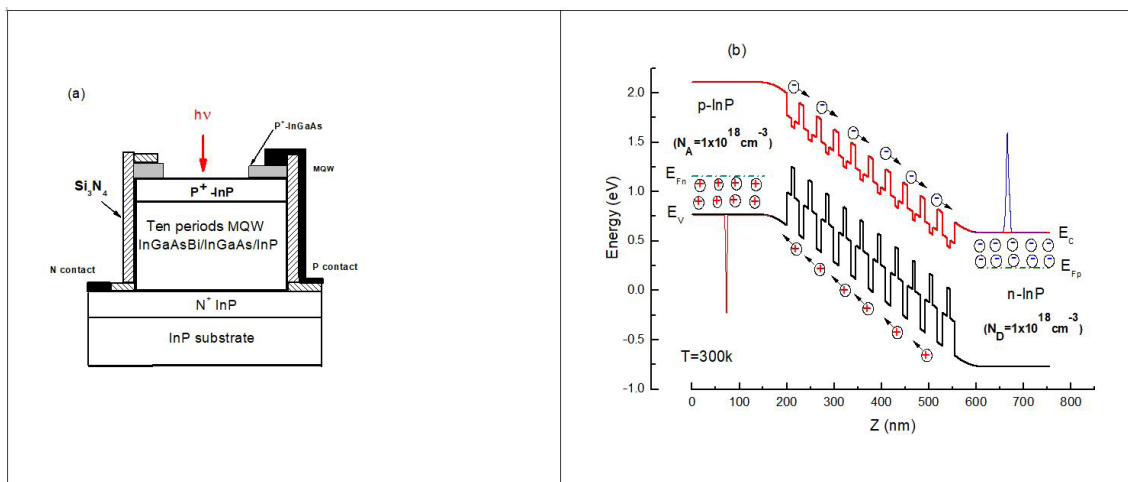
Figure 6: Room temperature evolution of the detection energies and the wavelength of radiation conforming to the edge of direct-band transitions of e_1–hh_1 versus the $In_{0.53}Ga_{0.47}As_{0.945}Bi_{0.055}$ layer thickness in $In_{0.53}Ga_{0.47}As_{0.945}Bi_{0.055}$/$In_{0.53}Ga_{0.47}As$/InP heterostructure. The inset is the calculated conduction and valence bands edges of the modeled structure schematized for the optimum parameters carrying out the transition with 2.6 μm wavelength

The $In_{0.53}Ga_{0.47}As_{0.945}Bi_{0.055}$/$In_{0.53}Ga_{0.47}$/InP quantum well device was studied with a p-i-n heterostructure, as exposed in Figure 7a. The p-i-n device commence with a 100 nm-thick n InP buffer layer strongly doped with Si to about ($N_D=1x10^{18}$ cm^{-3}), which too represented as the engraving top and bottom contact layer. A 265 nm-thick unintentionally doped n type MQWs $In_{0.53}Ga_{0.47}As_{0.945}Bi_{0.055}$/$In_{0.53}Ga_{0.47}$ absorption layer doped with Si to about ($N_D=1x10^{16}$ cm^{-3}). A 100 nm-thick p$^+$ InP window layer and a 50 nm-thick p$^+$ InGaAs top contact layer. Both heavily doped with Be to about ($N_A=1x10^{18}$ cm^{-3}). These layers were grown at the usual InP growth temperature. For simplicity, we overlook the effects of impurities or defects in the host lattice. The modeled p-i-n heterostructure of $In_{053}Ga_{0.47}As_{0.94}5Bi_{0.055}$/$In_{0.53}Ga_{0.47}As$/InP has to be calculated self-consistently. The Hamiltonian includes $V_B(z)$ represents the band discontinuities at the interfaces, $V_{XC}(z)$, the local exchange-correlation potential energy and Hartree potential acquired by resolving Poisson's equation. The relative wave functions Ψ_i and the eigenvalues E_i are determined starting from the results of Schrodinger's equation solutions assuming the effective mass approximation [43,44].

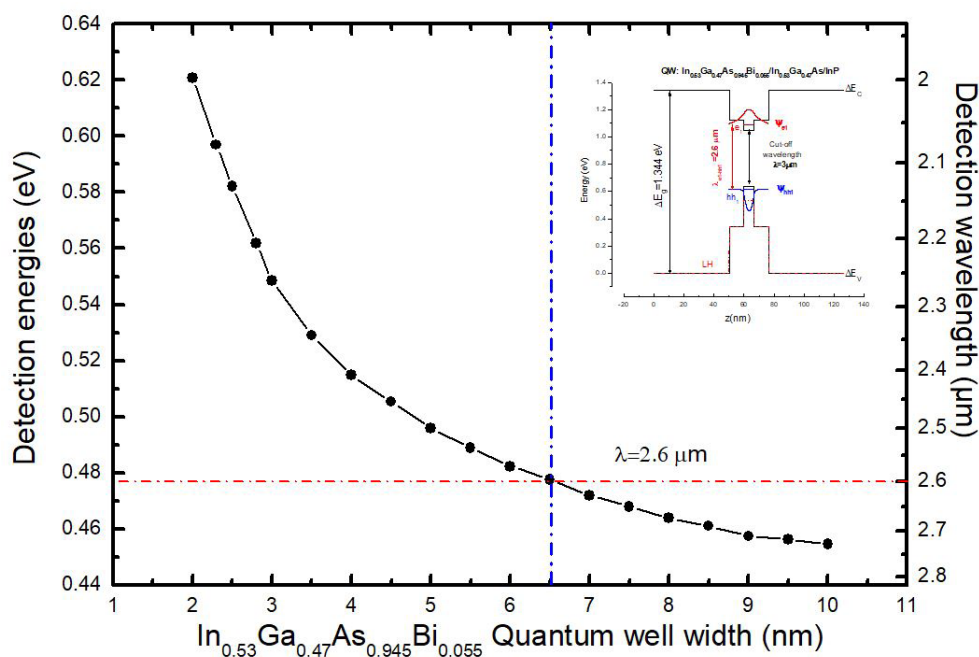**Figure 7: (a)** Schematic diagram of a p-i-n detector device; **(b)** The designed band profiles of the conduction and valence bands with an absorption zone containing on ten periods of $In_{053}Ga_{0.47}As_{0.945}Bi_{0.055}$/$In_{0.53}Ga_{0.47}As$/InP MQW p-i-n structure optimally designed for 2.6μm detection. The pseudo Fermi level and the relative wave functions are plotted at reversed bias -0.1V

$$\left(-\frac{\hbar^2}{2m_0} \frac{d}{dz} \left(\frac{1}{m(z)} \frac{d}{dz} \right) + V_B(z) + V_H(z) + V_{xc}(z) \right) \Psi_i(z) = E_i \Psi_i(z) \tag{28}$$

$$\varepsilon_0 \frac{d}{dz} \left[\varepsilon_r(z) \frac{d}{dz} V_H(z) \right] = e^2 [N_D(z) - N_A(z) + p(z) - n(z)] \tag{29}$$

For simplicity, we overlook the effects of impurities or defects in the host lattice. The p-i-n device structure is presented in Figure 7b that displays the calculated band edges corresponding to the valence and conduction bands with an absorption zone containing on 10 periods of $In_{053}Ga_{0.47}As_{0.945}Bi_{0.055}/In_{0.53}Ga_{0.47}As$ MQW structure optimally designed for 2.6 μm detection. Besides, the pseudo Fermi level and wave functions are plotted at reversed bias -0.1V. With the aim to simulate the dark current densities in the propounded hetrostrecture InGaAsBi/InGaAs/InP, five types of theoretical mechanisms models were highlighted respectively, diffusion currents densities (J_{Diff}) generation–recombination (J_{GR}) currents densities, the trap assisted tunneling current(J_{TAT}), band-to-band tunneling currents densities (J_{BTB}), currents densities and the tunneling currents densities through the barriers (J_T), whereas the conduction currents densities were logically ignored for this MQWs InGaAsBi/InGaAs/InP heterostructure. These currents densities are calculated using equations, according to the procedure outlined in references [45-47].

$$J_{diff} = n_i^2 \sqrt{qk_BT} \left(\frac{1}{N_A} \sqrt{\frac{\mu_e}{\tau_e}} + \frac{1}{N_D} \sqrt{\frac{\mu_h}{\tau_h}} \right) (e^{\frac{qV}{k_BT}} - 1) \tag{30}$$

$$J_{GR} = \frac{qn_i}{2\tau_{GR}} \sqrt{\frac{2\varepsilon_0\varepsilon_r(N_A + N_D)}{qN_AN_D}} \sqrt{V_t} (e^{\frac{qV}{2k_BT}} - 1) \tag{31}$$

$$J_{TAT} = \frac{q^2m_TVM^2N_t}{8\pi\hbar^3(E_g - E_t)} \exp(-\frac{4\sqrt{2m_T(E_g - E_t)^3}}{3q\hbar F(V)}) \tag{32}$$

$$J_{BTB} = \frac{q^3EV\sqrt{2m_e}}{4\pi^2\hbar\sqrt{E_g}} \exp(\frac{-4\sqrt{2m_e}E_g^{3/2}}{3qE\hbar}) \tag{33}$$

$$J_T = \frac{em_i^*k_BT}{2\pi^2\hbar^3} \int_0^\infty T(E,V)Ln \left[\frac{1 + \exp(E_f - E/k_BT)}{1 + \exp(E_f - E - eV/k_BT)} \right] dE \tag{34}$$

Where q is the electron charge, N_A and N_D are, respectively, the p and n-type doping concentrations, T is the temperature, μ_e, τ_e and μ_h, τ_h are the mobilities and lifetimes of electrons and holes, respectively, τ_{GR} is the generation-combination lifetime, ε_s is the static dielectric constant, ε_r is the relative effective dielectric constant value of the multilayer InGaAsBi/InGaAs/InP, ε_0 is the permittivity of free space, $V_t = V_d - V$ is the total junction potential, V is the bias voltage, V_d is the built-in potential of the heterostructure, k_B is the Boltzmann constant, F is the applied electric field, $\hbar$ is the Planck constant, m_T is the reduced tunneling effective mass, E_g is the band gap, d is the thickness of the n zone, L_h is the hole diffusion length and N_T is the activated trap density which is given below :

$$N_T = \frac{\left\{ \left(\frac{\partial^2 I_{dif}}{\partial V^2} \right) + \left(\frac{\partial^2 I_{gr}}{\partial V^2} \right) \right\}_{V=V_m}}{\frac{2q^3 A \pi^2 m_e M^2}{h^3 (E_g - E_t)} \exp\left(-\frac{B}{V_t^{1/2}} \right)_{V=V_m} \left(\frac{B}{4V_t^{1/2}} + \frac{B^2}{4V_t^2} \right)_{V=V_m}}$$

(35)

$$B = \frac{8\pi (2m_e)^{1/2} (E_g - E_t)^{3/2}}{\left\{ 3qh \left(\frac{2qN_D}{\varepsilon_0 \varepsilon_s} \right)^{1/2} \right\}}$$

(36)

E_t is the trap energy location, n_i represents the intrinsic carrier concentration inside the quantum well InGaAsBi/InGaAs/InP, M^2 is a matrix element related with the trap potential and V_m corresponds to the value of applied voltage V at the peak position. In Table 3, we summarize the essential parameters adopted in this simulation work. These parameters are taken from References [48-53].

Parameters	Values
Mobility electrons μ_n	3000 cm²/Vs
Mobility holes μ_p	1000 cm²/Vs
Diffusion coefficient electrons D_n	75 cm²/s
Diffusion coefficient holes D_p	25 cm²/Vs
The trap density N_t	2×10^{11}cm⁻³
The trap energy location E_t	0.58eV
Lifetimes of electrons τ_n	3×10^{-12}s
Lifetimes of holes τ_p	1×10^{-12}s
The generation-combination lifetime τ_{GR}	5×10^{-12}s
The matrix element M^2	1×10^{-23}eV²cm
The intrinsic carrier concentration n_i	8.45×10^8cm⁻³
Refractive index n	2.0542

Table 3: Parameters used in the calculations of dark current and quantum efficiency at 300 K. They are taken from References [48-53]

The Figure 8a illustrates the dark current density-voltage characteristics $(J - V)$ of the 100 μm diameter detector as function of temperatures ranging from 77 to 300 K. The Detector rectification behavior has been observed for different temperatures. As can be seen that the current density increases with temperature increasing. The current density of InGaAsBi/InGaAs detector at 300K is about 5.38×10^{-5}A/cm² at -10mV, which is almost less than about four and a half times of the value find experimentally by Gu et al (2.4×10^{-4}A/cm²) for the InGaAsBi detector at the same temperature the results are outline in ref [18]. As temperature decreases, the dark current density decreases to 5.93×10^{-7}A/cm² at 77k. Dotted lines in the presentation are the modeled values find based on the equations mention above. To understanding the contribution of different mechanisms, such as diffusion, generation-recombination, trap-assisted-tunneling, and the Ohmic-type defect-related leakage. At 77k and under zero bias the dark current density is about of 3.09×10^{-7}A/cm² agreeing to a differential-resistance-area-product at zero bias of $1.62 \times 10^7 \, \Omega$ cm². The profile of the $R_0 A$ as function of $1/T$ presentation in Figure 8b as well as the calculated values show that the dark current is conquered by three diverse mechanisms in three different temperature regimes. From 77 to 100 K, the detector performance is

restricted by the temperature-insensitive defect-related leakage [54]. That incites amelioration in the characteristics of InGaAsBi/InGaAs detector by comparison with the InGaAs detectors [55]. This performance can be explained by the modification caused by the addition of bismuth at the level of the valence band. Beyond 100 K, the thermally generated carriers build a durable generation-recombination and diffusion current that bigger than the defect-leakage current. From 100 to 200 K, the InGaAsBi/InGaAs detector in the beginning is limited by the generation-recombination process, and after that the diffusion current density be appointed as the influential one. In the temperature range higher than 200 K, the thermal recombination current seems to be the main dark current mechanism. From 300k the conduction mechanism starts to appear. The contribution of each mechanisms participating in the calculation of the dark current density is given by Figure 9a.
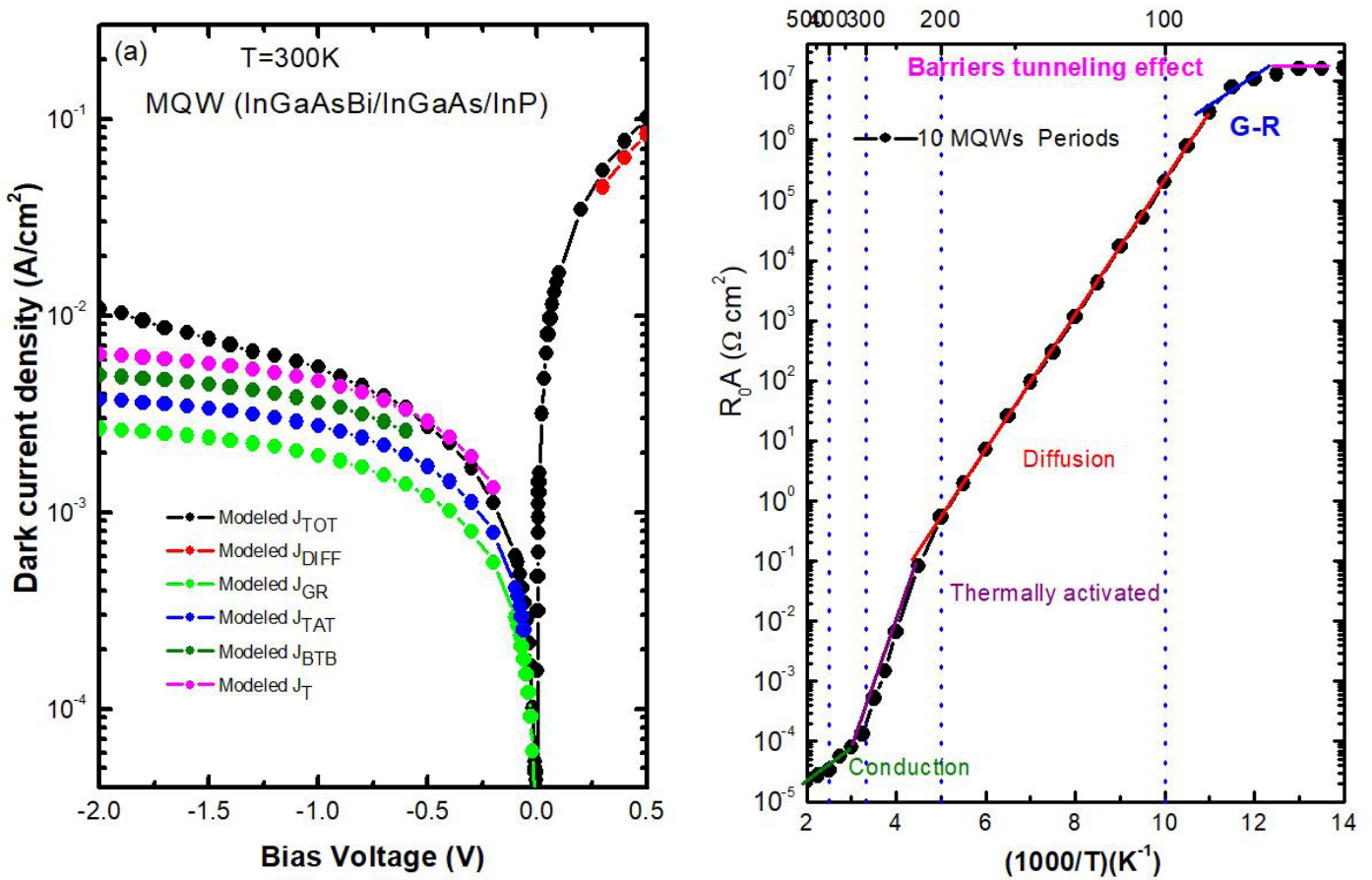

Figure 8: (Color online) **(a)** The bias-dependent dark current density J(V) for diverse temperatures on 100 µm diameter of the InGaAsBi/InGaAs/InP detector, dotted lines are modeled values and **(b)** R_0A as a function of $1/T$ relation shows five distinct regimes with different dominant mechanisms: barriers tunneling effect, generation-recombination, diffusion, generation-recombination, thermally activated and conduction
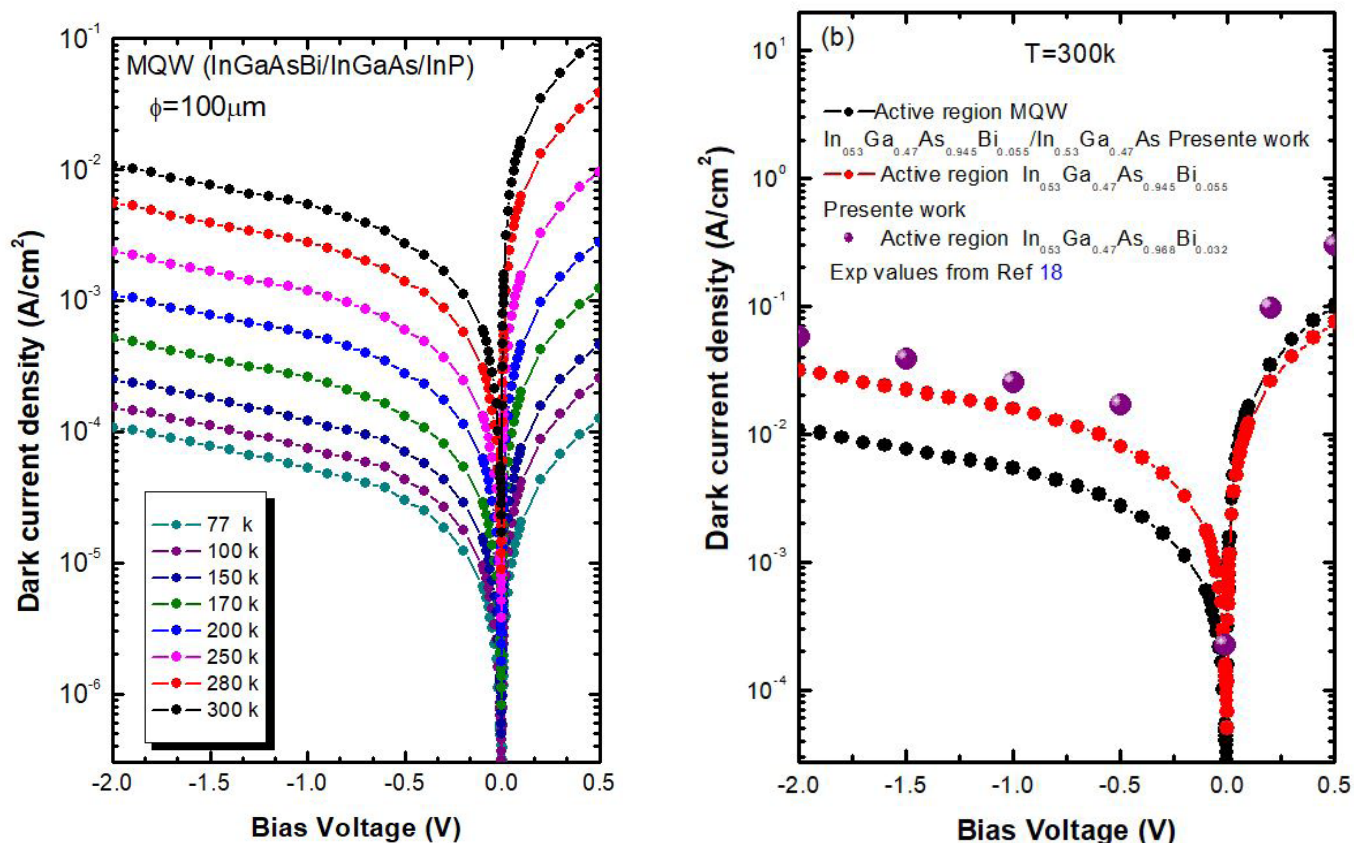
Figure 9: (a) Total dark current density at 300 K versus bias voltage from −2 V to 0.5 V is presented with five distinct regimes with different dominant mechanisms, the diffusion currents densities, Generation-recombination currents densities, Trapp assisted tunneling currents densities, band-to-band tunneling currents densities and the tunneling currents densities through the barriers; **(b)** Dark current density–voltage characteristics of InGaAsBi p-i-n detector with Bi compositions of 5.5% and 3.2%, for devices with different active region MQW $In_{053}Ga_{0.47}As_{0.945}Bi_{0.055}/In_{0.53}Ga_{0.47}As$ and $In_{053}Ga_{0.47}As_{0.945}Bi_{0.055}$. The symbols are the experimental data of $In_{053}Ga_{0.47}As_{0.968}Bi_{0.032}$ active region taken from [18]

In order to highlight the technological advantage of using MQW $In_{053}Ga_{0.47}As_{0.945}Bi_{0.055}/In_{0.53}Ga_{0.47}As$, as active zone in one hand we have make comparison of dark current density voltage $(J − V)$ characteristics calculated at RT between bulk $In_{053}Ga_{0.47}As_{0.945}Bi_{0.055}$ and $In_{053}Ga_{0.47}As_{0.945}Bi_{0.055}/In_{0.53}Ga_{0.47}As$ MQW active regions.

The calculated dark current acquired for a 100 μm thick bulk $In_{053}Ga_{0.47}As_{0.945}Bi_{0.055}$ active region, witch device has a typical dark-current of 1.75×10^{-3}A/cm^2 at -0.1V .The employ of MQW as the active zone decreases the dark current around 6×10^{-4}A for the same reverse voltage.

In the other hand the use of 3.2% as Bi content for experimental device with $In_{053}Ga_{0.47}As_{0.968}Bi_{0.032}$ active region [18] represented a typical dark current density of 2.4×10^{-4}A/cm^2 at reverse bias voltage of 10mV at 300 K, in the same applied voltage the dark current is about 5.38×10^{-5}A/cm^2 for the device made with MQW.

$In_{053}Ga_{0.47}As_{0.945}Bi_{0.055}/In_{0.53}Ga_{0.47}As$ as active zone. These results are summarized in Figure 9b. The dark current density designates the quality of the material, as wells as the optical sensitivity of the device. In Figure 10 the quantum efficiency has been calculate versus the wavelength at different temperatures with the analytic model, based on the Hovel's formula [56,57]. The QE of p-i-n structure is defined as the addition of the contributions from three zones: The n doped region (QE_n), the p doped region (QE_p) and the space charge region (QE_{sc}) using the following expression:
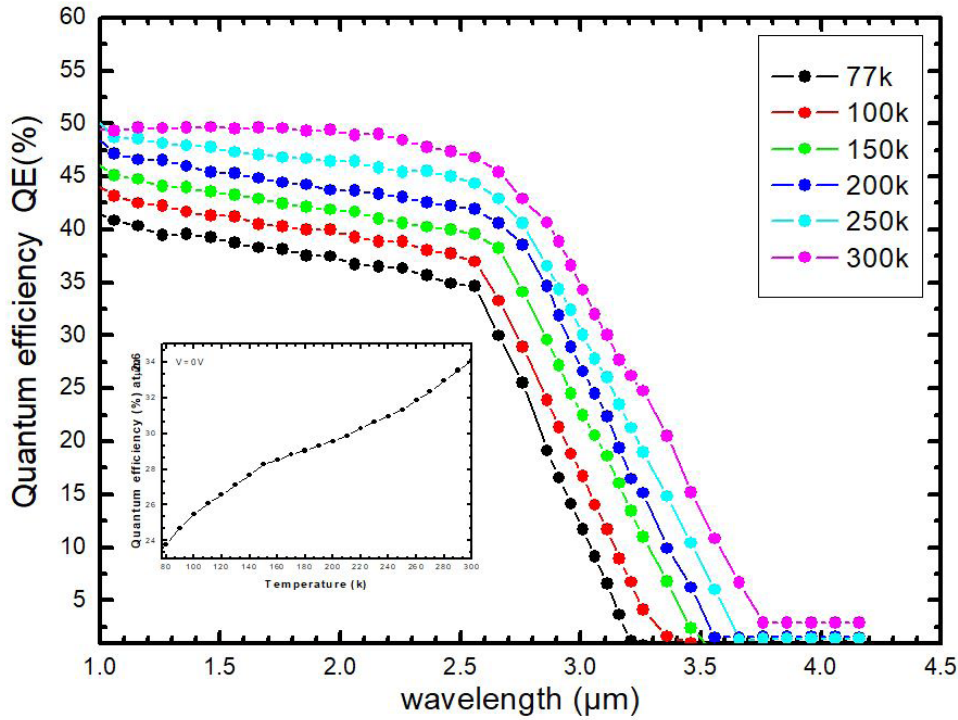
Figure 10: (Color online) the wavelength-dependent modeled quantum efficiency spectrums of the devices versus different temperatures at zero bias. The inset is the quantum efficiency at 2.6 μm versus temperature

$$QE = QE_n + QE_{SCR} + QE_p \tag{37}$$

$$QE_{SCR} = (1 - R) \times (\exp(-\alpha x_1) - \exp(-\alpha x_2)) \tag{38}$$

$$QE_n = \frac{(1-R)\alpha L_h}{\alpha^2 L_h^2 - 1} \exp(-\alpha x_2) \left[\frac{\alpha L_h + \gamma_1 - \exp(-\alpha(x_{max}-x_2)) \left[\gamma_1 \cosh\left(\frac{(x_{max}-x_2)}{L_h}\right) + \sinh\left(\frac{(x_{max}-x_2)}{L_h}\right) \right]}{\gamma_1 \sinh\left(\frac{(x_{max}-x_2)}{L_h}\right) + \cosh\left(\frac{(x_{max}-x_2)}{L_h}\right)} - \alpha L_h \exp\left(-\alpha(x_{max}-x_2)\right) \right] \tag{39}$$

$$QE_p = \frac{(1-R)\alpha L_e}{\alpha^2 L_e^2 - 1} \left[\frac{(\gamma_2 - \alpha L_e)e^{-\alpha x_1} - \sinh\left(\frac{x_1}{L_e}\right) - \gamma_2 \cos\left(\frac{x_1}{L_e}\right)}{\cosh\left(\frac{x_1}{L_e}\right) - \gamma_2 \sinh\left(\frac{x_1}{L_e}\right)} + \alpha L_e \right] \tag{40}$$

$$\gamma_1 = \frac{S_n L_n}{D_n} \text{ and } \gamma_2 = \frac{S_p L_h}{D_p} \tag{41}$$

$$R = \frac{(n_2 - n_1)^2}{(n_2 + n_1)^2} \tag{42}$$

$$L_e = \sqrt{D_n \tau_n} = \sqrt{\frac{kT}{q} \mu_n \tau_n} \tag{43}$$

$$L_h = \sqrt{D_p \tau_p} = \sqrt{\frac{kT}{q} \mu_p \tau_p} \tag{44}$$

where, Sn and Sp are the recombination velocities in regions p and n respectively. n_1 and n_2 are the refractive index of $In_{0.53}Ga_{0.47}As_{0.945}Bi_{0.055}$ and $In_{0.53}Ga_{0.47}As$ respectively [58, 60]. The temperature dependence quantum efficiency is presented in Figure 10 versus wavelength detection. It is clear in Figure 10, that the cut-off wavelength of the detector changes from 3 to 3.3 μm once the temperature enhanced from 77 K to 300 K. At zero bias the quantum efficiency increases with temperature (seen the inset of Figure 10), it has been predicted to be 46.7% at 300 K for λ = 2.6 μm but its value droplets after 2.6 μm wavelength. The

detectivity D^* is one of the key parameters to highlight the proposed $In_{0.53}Ga_{0.47}As_{0.945}Bi_{0.055}/In_{0.53}Ga_{0.47}As$ detector structure. The conventional expression of detectivity D^* can be given by this following formula taken from ref [60]:

$$D^* = \lambda \frac{q}{hc} QE \sqrt{\frac{R_0 A}{4 k_B T}}$$

(45)

The calculated detectivity D^* as the function of wavelength at zero bias is represented in Figure 11. It can be seen that the detectivity increases through increase in detection wavelength. It arrives at a peak value at λ = 2.6 µm then after falls speedily with more increase in wavelength. At RT, the devise shows a great value of detectivity of about 4.5 10^{11} cm Hz$^{1/2}$W^{-1} in the wavelength range 1–4 µm. The predicted detectivity for the suggested InGaAsBi/InP device showed similar performance to type-II InAs/GaSb superlattice photodiodes [61] and MIR detectors founded with other material compounds [62]. At 77 K, the modeled device attains with detectivity about 4.4 10^{12} cmHz$^{1/2}$W^{-1} which is four orders of magnitude higher than the one found by Levine et al. [63]. The dark current results from the interchange between the doping ionized impurities and the electron for this raisin it is required to retain the doping concentration in the active zone in order to approve a high detectivity at RT. From our calculated results of detectivity in the modeled devise, around 4.3 10^{11} cm Hz$^{1/2}$W^{-1} in the wavelength range 1–2.75µm at RT.
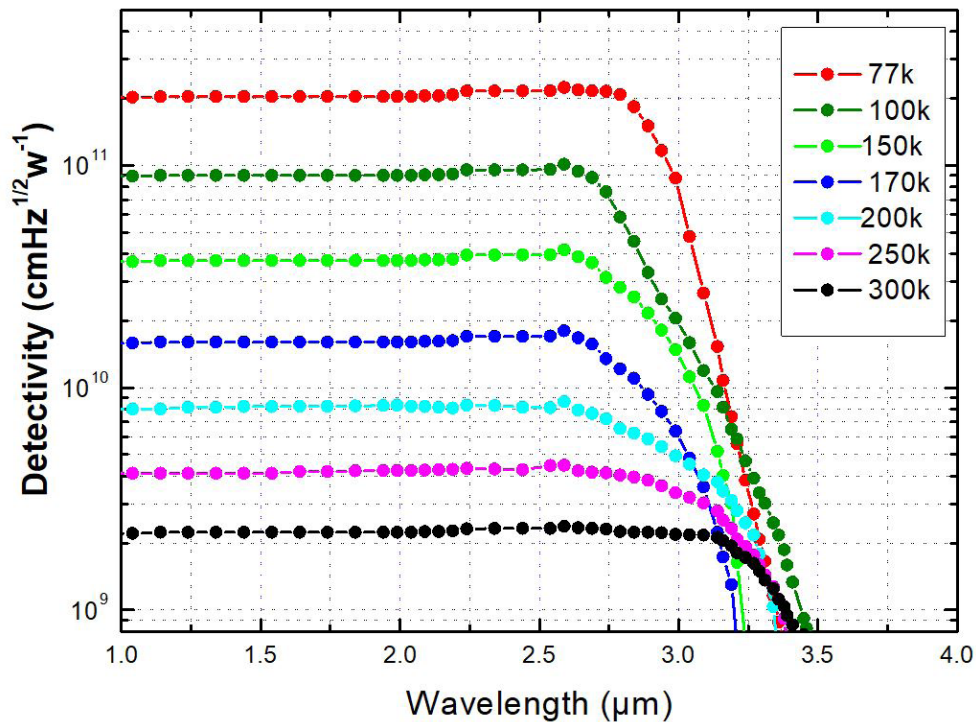

Figure 11: (Color online) Calculated detectivity as function of wavelength at zero bias of the device at different temperatures

In order to investigate the potential application of InGaAsBi/InGaAs/InP p-i-n devices. We have calculated the optical responsivity achieved with the use the following expression [64]:

$$R(\lambda) = \frac{\eta_i q \lambda \, \Omega}{h} \frac{\Gamma \alpha(\lambda, V)}{\Gamma \alpha(\lambda, V) + \alpha_i} (1 - \exp(-(\alpha_i + \Gamma \alpha(\lambda, V) \, L))$$

(46)

where η_i represents the internal quantum efficiency, Γ is the confinement factor of the optical mode within the MQW heterostructure, $\alpha(\lambda, V)$ refers to the absorption coefficient at wavelength λ and bias V, L is the waveguide length, and Ω is the coupling efficiency, including mode size mismatch and reflection [65] α_i ($\alpha_i = 120\,cm^{-1}$) represents all propagation losses that do not generate photocurrent. The quantum efficiency η_i is correlated to absorption coefficient α and thickness d of the absorption layer ($\eta_i = 1 - exp(-\alpha d)$). We have theoretically calculated the coefficient $\alpha(\lambda, V)$ in accordance with the equation described

in our antecedent work [66]. At RT, the responsivity has been calculated for different reverse bias voltages (0 V, -0.5 V and -1 V) who's the results are exhibited in Figure 12. This responsivity versus wavelength (2–3.4 μm) spreads a peak. This peak matches to the e_1-hh_1 transition energy and the strained direct band gap of $In_{053}Ga_{0.47}As_{0.945}Bi_{0.055}/In_{0.53}Ga_{0.47}As$ QWs; are observed around 2.6 μm. By the same token, we can easily note that the responsivity increases once the reverse bias voltage is elevated. In the case of a reverse bias voltage of -1 V, we obtain the responsivities of 0.807 A/W at 2.6 μm at RT. The responsivity of the InGaAsBi/InGaAs/InP detector was 0.77 A/W, corresponding to the external quantum efficiency of about 46.7%. The resistance area product R_0A of the structure at zero bias was similarly calculated at RT is 5.75×10^{-4} Ωm^2. On the basis of the calculated R_0A and the external quantum efficiency, the detectivity at 2.6 μm and RT was deduced to be 2.38×10^9 cmHz$^{1/2}$/W. Consequently, these theoretical results show that these novel dilute-bismuth InGaAsBi/InGaAs/InP detectors could be used for RT shortwave infrared applications.
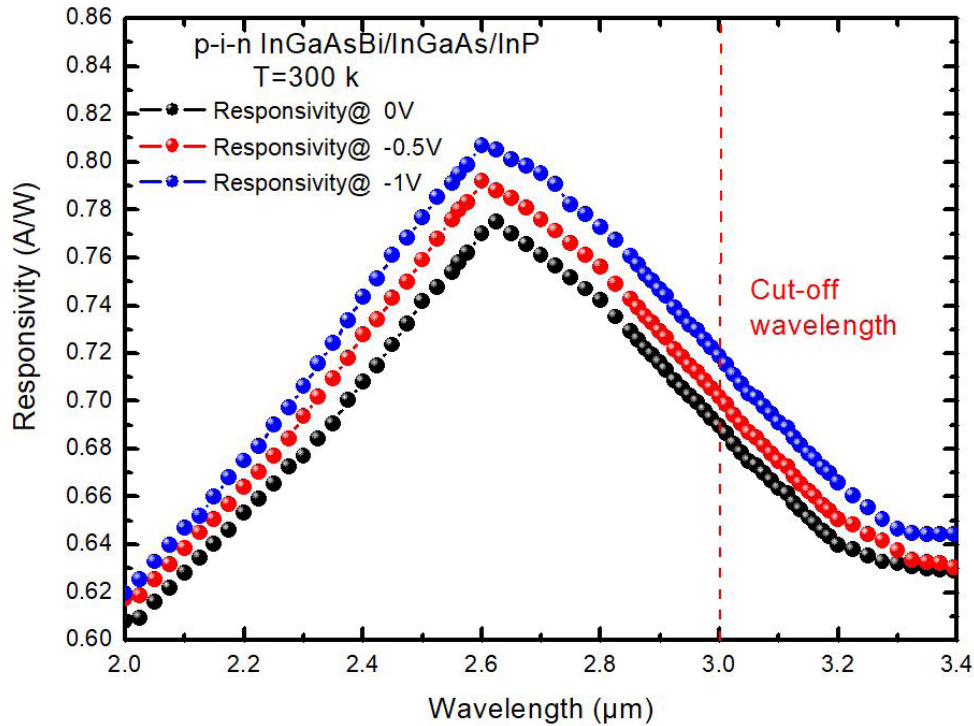

Figure 12: Optical responsivity from λ = 2 μm to λ = 3.4 μm for the InGaAsBi/InGaAs/InP p-i-n detectors at 0, −0.5 and −1 V, respectively

In addition to optical communication, this type of devices would also be suitable for detection applications because of their higher electro-optical characteristics, specifically low dark current, greater sensitivity, high quantum efficiency and swift response

Conclusion

In summary, the quantum engineering of band parameters are a powerful tool to investigate dilute bismuth InGaAsBi alloys. The band gap, band discontinuities and spin-orbit splitting energy of InGaAsBi/InP have been studied in order to achieve dilute bismuth optoelectronic devices. It is clearly apparent that InGaAsBi alloys are encouraging for near- and mid-infrared detector devices due to the flexibilities of the control of same parameters such as the band discontinuities and spin-orbit splitting. We have demonstrated the InGaAsBi/InGaAs detector, in which the complete heterostructure is nearly lattice-matched to InP substrate. The Bi fraction is about 5.5% in the absorption layer and the cut-off wavelength has been protracted to 3μm at RT, matching to a Bi-induced bandgap reduction of about 362meV. The simulation of detector performance based on $In_{0.53}Ga_{0.47}As_{0.945}Bi_{0.055}/In_{0.53}Ga_{0.47}/InP$ multi quantum wells has been studied for high temperature operation. The electrical and optical properties (dark current and resistance area product) and (quantum efficiency, responsivity, and detectivity) respectively of the detector have been studied versus a wide range of temperatures and bias voltages, which is essential for examining mechanisms of carrier transport through the modeled p-i-n device. These results prove that InP-based diluted bismide InGaAsBi material is a potential candidate emerging as a promising candidate for the spreading of short wavelength infrared detectors.

References

1. Tixier S, Adamcyk M, Tiedje T, Francoeur S, Mascarenhas A, et al. (2003) Molecular beam epitaxy growth of GaAs1−xBix. Appl Phys Lett 82: 2245.

2. Francoeur S, Seong MJ, Mascarenhas A, Tixier S, Adamcyk M, et al. (2003) Band gap of GaAs1−xBix, 0<x<3.6%. Appl Phys Lett 82: 3874.

3. Lu X, Beaton DA, Lewis RB, Tiedje T, Whitwick MB (2008) Effect of molecular beam epitaxy growth conditions on the Bi content of GaAs1−xBix. Appl Phys Lett 92: 192110.

4. Carrier P, Wei SH (2004) Calculated spin-orbit splitting of all diamondlike and zinc-blende semiconductors: Effects of p1/2 local orbitals and chemical trends. Phys Rev B 70: 035212.

5. Fluegel B, Francoeur S, Mascarenhas A, Tixier S, Young EC, et al. (2006) Giant spin-orbit bowing in GaAs1-xBix. Phys Rev Lett 97: 067205.

6. Alberi K, Wu J, Walukiewicz W, Yu KM, Dubon OD, et al. (2007) Valence-band anticrossing in mismatched III-V semiconductor alloys. Phys Rev B 75: 045203.

7. Marko IP, Batool Z, Hild K, Jin SR, Hossain N, et al. (2012) Temperature and Bi-concentration dependence of the bandgap and spin-orbit splitting in InGaBiAs/InP semiconductors for mid-infrared applications. Appl Phys Lett 101: 221108.

8. Jin SR, Sweeney SJ (2013) InGaAsBi alloys on InP for efficient near- and mid-infrared light emitting devices. J Appl Phys 114: 213103.

9. Rajpalke MK, Linhart WM, Birkett M, Yu KM, Scanlon DO, et al. (2013) Growth and properties of GaSbBi alloys. Appl Phys Lett 103: 142106.

10. Song YX, Wang SM, Roy IS, Shi PX, Hallen A, et al. (2013) Molecular beam epitaxy growth of InSb1−xBix thin films. J Cryst Growth 378: 323-8.

11. Huang KT, Chiu CT, Cohen RM, Stringfellow GB (1994) InAsSbBi alloys grown by organometallic vapor-phase epitaxy. J Appl Phys 75: 2857.

12 Zhou Z, Mendes DF, Richards RD, Bastiman F, David JPR (2015) Absorption properties of GaAsBi based p–i–n heterojunction diodes. Semicond Sci Technol 30: 094004.

13. Sandall IC, Bastiman F, White B, Richards R, Mendes D, et al. (2014) Demonstration of InAsBi photoresponse beyond 3.5 μm. Appl Phys Lett 104: 171109.

14. Hoogeveen RWM, Vander ARJ, Goede APH (2001) Extended wavelength InGaAs infrared (1.0–2.4 μm) detector arrays on SCIAMACHY for space-based spectrometry of the Earth atmosphere. Infrared Phys Technol 42: 1-16.

15. Zhang YG, Gu Y, Tian ZB, Li AZ, Zhu XR, et al. (2008) Wavelength extended 2.4 μm heterojunction InGaAs photodiodes with InAlAs cap and linearly graded buffer layers suitable for both front and back illuminations. Infrared Phys Technol 51: 316.

16. Gu Y, Zhou L, Zhang YG, Chen XY, Ma YJ, et al. (2015) Dark current suppression in metamorphic In0.83Ga0.17As photodetectors with In0.66Ga0.34As/InAs superlattice electron barrier. Appl Phys Express 8: 022202.

17. Petropoulos JP, Zhong Y, Zide JMO (2011) Optical and electrical characterization of InGaBiAs for use as a mid-infrared optoelectronic material. Appl Phys Lett 99: 031110.

18. Gu Y, Zhang YG, Chen XY, Ma YJ, Xi SP, et al. (2016) Nearly lattice-matched short-wave infrared InGaAsBi detectors on InP. Appl Phys Lett 108: 032102.

19. Zhong Y, Dongmo PB, Petropoulos JP, Zide JMO (2012) Effects of molecular beam epitaxy growth conditions on composition and optical properties of InxGa1−xBiyAs1−y. Appl Phys Lett 100: 112110.

20. Devenson J, Pacebutas V, Butkute R, Baranov A, Krotkus A (2012) Structure and Optical Properties of InGaAsBi with up to 7% Bismuth. Appl Phys Express 5: 015503.

21. Gu Y, Zhang YG, Chen XY, Ma YJ, Xi SP, et al. (2016) Nearly lattice-matched short-wave infrared InGaAsBi detectors on InP. Appl Phys Lett 108: 032102.

22. Tian F, Ai L, Xu A, Huang H, Qi M (2021) InGaAsPBi grown on InP substrate by gas source molecular beam epitaxy. Materials Research Express 8: 026404.

23. Sweeney JS, Eales TD, Marko IP (2020) Materials, Devices and applications. Mid-infrared Optoelectronics 3: 56.

24. Sfina N, Ammar I, Lazzari J-L, Said M (2020) Modelization of electrical and optical characteristics of short-wave infrared type I InGaAsBi/InGaAs/InP quantum wells p-i-n detector. Physica Scripta 96: 035802.

25. Pavelescu EM, Ligor O, Occena J, Ticoş C, Matei A, et al. (2020) Influence of electron irradiation and rapid thermal annealing on photoluminescence from GaAsNBi alloys. Appl Phys Lett 117: 142106.

26. Mal I, Samajdar DP (2020) InSbNBi/InSb heterostructures for long wavelength infrared photodetector applications: A 16 band k·p study. J Appl Phys 128: 095701.

27. Petropoulos JP, Zhong Y, Zide JMO (2011) Optical and electrical characterization of InGaBiAs for use as a mid-infrared optoelectronic material. Appl Phys Lett 99: 031110.

28. Kudrawiec R, Kopaczek J, Misiewicz J, Walukiewicz W, Petropoulos JP, et al. (2012) Temperature dependence of E0 and E0 + ΔSO transitions in In0.53Ga0.47BixAs1−x alloys studied by photoreflectance. J Appl Phys 112: 113508.

29. Jin SR, Sweeney SJ (2013) InGaAsBi alloys on InP for efficient near- and mid-infrared light emitting devices. J Appl Phys 114: 213103.

30. Souto S, Hilska J, Galvão Gobato Y, Souza D, Andrade MB, et al. (2020) Raman spectroscopy of GaSb1−xBix alloys with high Bi content. Appl Phys Lett 116: 202103.

31. Dongmo P, Zhong YJ, Attia P, Bomberger C, Cheaito R, et al. (2012) Enhanced room temperature electronic and thermoelectric properties of the dilute bismuthide InGaBiAs. J Appl Phys 112: 093710.

32. Butkute R, Pacebutas V, Cechavicius C, Nedzinskas R, Selskis A, et al. (2014) Photoluminescence at up to 2.4 μm wavelengths from GaInAsBi/AlInAs quantum wells. J Cryst Growth 391: 116-20.

33. Kasap S, Capper P (2006) Springer Handbook of Electronic and Photonic Materials, New York: Springer, USA.

34. Assalia AB, Bouslama MH, Reshak AH, Chaabanee L (2017) Highly desirable semiconducting materials for mid-IR optoelectronics: Dilute bismide InAs1−xBix alloys. Mater Res Bull 95: 588-96.

35. Madouri D, Boukra A, Zaoui A, Ferhat M (2008) Bismuth alloying in GaAs: a first-principles study. Computational Materials Science 43: 818-22.

36. Chai GMT, Broderick CA, O'Reilly EP, Othaman Z, Jin SR, et al. (2015) Experimental and modelling study of InGaBiAs/InP alloys with up to 5.8% Bi, and with Δso > Eg. Semicond Sci Technol 30: 094015.

37. Van de Walle CG, Martin RM (1986) Theoretical calculations of heterojunction discontinuities in the Si/Ge system. Phys Rev B 34: 5621.

38. Van de Walle CG (1989) Band lineups and deformation potentials in the model-solid theory. Phys Rev B 39: 1871.

39. Usman M, Broderick CA, Lindsay A, O'Reilly EP (2011) Tight-binding analysis of the electronic structure of dilute bismide alloys of GaP and GaAs. Phys Rev B 84: 245202.

40. Jin SR, Sweeney SJ (2013) InGaAsBi alloys on InP for efficient near- and mid-infrared light emitting devices. J Appl Phys 114: 213103.

41. Estrada-Delgado MI, Fernandez DJ (2019) Ladder operators for the BenDaniel-Duke Hamiltonians and their SUSY partners. Eur Phys J 134: 341.

42. Stern F, Sarma SD (1984) Electron energy levels in GaAs-Ga1−xAlxAs heterojunctions. Phys Rev B 30: 840.

43. Ando T, Fowler AB, Stern F (1982) Electronic properties of two-dimensional systems. Rev Mod Phys 54: 437.

44. Yang QK, Fuchs F, Schmitz J, Pletschen W (2002) Investigation of trap-assisted tunneling current in InAs/(GaIn)Sb superlattice long-wavelength photodiodes. Appl Phys Lett 81: 4757.

45. Wong JY (1980) Effect of trap tunneling on the performance of long-wavelength Hg1-xCdxTe photodiodes. IEEE Trans. Electron Devices ED 27: 48.

46. Kinch MA (1982) Electronic properties of HgCdTe. J Vac Sci Technol 21: 215.

47. Baker IM, Maxey CD (2001) Summary of HgCdTe 2D array technology in the U.K. J Electron Mater 30: 682.

48. Gozu S-I, Mozume T, Ishikawa H (2008) Refractive index of Si-doped n-InGaAs. J App Phys 104: 073507.

49. Verdun M, Beaudoin G, Portier B, Bardou N, Dupuis C, et al. (2016) Dark current investigation in thin P-i-N InGaAs photodiodes for nano-resonators. J App Phys 120: 084501.

50. Piprek J (2018) Handbook of Optoelectronic Device Modeling and Simulation, by Taylor and Francis Group, USA.

51. Chen XY, Gu Y, Zhang YG, Xi SP, Du B, et al. (2016) Characteristics of InGaAsBi with various lattice mismatches on InP substrate. AIP Adv 6: 075215.

52. Jin SR, Sweeney SJ (2013) InGaAsBi alloys on InP for efficient near- and mid-infrared light emitting devices. J Appl Phys 114: 213103.

53. Kinch MA (1982) Electronic properties of HgCdTe. J Vac Sci Technol 21: 215.

54. Zhang YG, Gu Y, Zhu C, Zhu GQ, Li AZ, et al. (2006) Gas source MBE grown wavelength extended 2.2 and 2.5 μm InGaAs PIN photodetectors. Infrared Phys Technol 47: 257-62.

55. Hovel H (1975) Semiconductors and Semimetals, Academic Press, New York, USA.

56. Aifer EH, Tischler JG, Warner JH, Vurgaftman I, Bewley WW, et al. (2006) W-structured type-II superlattice long-wave infrared photodiodes with high quantum efficiency. Appl Phys Lett 89: 053519.

57. Michel E, Razeghi M (1998) Recent advances in Sb-based materials for uncooled infrared photodetectors. Optoelectron Rev 6: 11.

58. Gozu S-I, Mozume T, Ishikawa H (2008) Refractive index of Si-doped n-InGaAs. J App Phys 104: 073507.

59. Aspnes DE, Studna AA (1983) Dielectric functions and optical parameters of Si, Ge, GaP, GaAs, GaSb, InP, InAs, and InSb from 1.5 to 6.0 eV. Phys Rev B 27: 985.

60. Nguyen BM, Hoffman D, Kwei-wei Huang E, Bogdanov S, Pierre-Yves D, et al. (2009) Demonstration of midinfrared type-II InAs/GaSb superlattice photodiodes grown on GaAs substrate. J App Phys 94: 223506.

61. Nguyen BM, Hoffman D, Kwei-wei Huang E, Bogdanov S, Pierre-Yves D, et al. (2009) Demonstration of midinfrared type-II InAs/GaSb superlattice photodiodes grown on GaAs substrate. J App Phys 94: 223506.

62. Zeiri N, Sfina N, Abdi-Ben Nasrallah S, Lazzari JL, Said M (2013) Intersubband transitions in quantum well mid-infrared photodetectors. Infrared Physics & Technology 60: 137.

63. Wu W, Bonakdar A, Mohseni H (2010) Plasmonic enhanced quantum well infrared photodetector with high detectivity. Appl Phys Lett 96: 161107.

64. Yahyaoui N, Sfina N, Lazzari JL, Bournel A, Said M (2015) Performance evaluation of high-detectivity p-i-n infrared photodetector based on compressively-strained Ge0.964Sn0.036/Ge multiple quantum wells by quantum modelling. Semicond Sci Technol 30: 085016.

65. Yoshimoto M (2019) Applications of Bismuth-Containing III-VSemiconductors in Devices. Molecular Beam Epitaxy 381: 394.

66. Yahyaoui N, Sfina N, Abdi-Ben Nasrallah S, Lazzari JL, Said M (2014) Electron transport through cubic InGaN/AlGaN resonant tunneling diodes. Comput Phys Commun 185: 3119.

Submit your next manuscript to Annex Publishers and benefit from:

› Easy online submission process
› Rapid peer review process
› Online article availability soon after acceptance for Publication
› Open access: articles available free online
› More accessibility of the articles to the readers/researchers within the field
› Better discount on subsequent article submission

Submit your manuscript at
http://www.annexpublishers.com/paper-submission.php